

# High-gain low-excess-noise MWIR detection with a 3.5- $\mu\text{m}$ cutoff AlInAsSb-based separate absorption, charge, and multiplication avalanche photodiode

Cite as: APL Photonics **8**, 036101 (2023); <https://doi.org/10.1063/5.0136918>

Submitted: 29 November 2022 • Accepted: 13 February 2023 • Accepted Manuscript Online: 13 February 2023 • Published Online: 03 March 2023

 Adam A. Dadey,  J. Andrew McArthur,  Abhilasha Kamboj, et al.



View Online



Export Citation



CrossMark

## ARTICLES YOU MAY BE INTERESTED IN

[A broadband high-brightness quantum-dot double solid immersion lens single photon source](#)

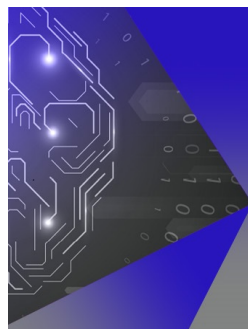
APL Photonics **8**, 036102 (2023); <https://doi.org/10.1063/5.0132161>

[AlInAsSb avalanche photodiodes on InP substrates](#)

Applied Physics Letters **118**, 091101 (2021); <https://doi.org/10.1063/5.0039399>

[Extremely low excess noise avalanche photodiode with GaAsSb absorption region and AlGaAsSb avalanche region](#)

Applied Physics Letters **122**, 051103 (2023); <https://doi.org/10.1063/5.0139495>



## APL Machine Learning

Machine Learning for Applied Physics  
Applied Physics for Machine Learning

**First Articles  
Now Online!**

# High-gain low-excess-noise MWIR detection with a 3.5- $\mu\text{m}$ cutoff AlInAsSb-based separate absorption, charge, and multiplication avalanche photodiode

Cite as: APL Photon. 8, 036101 (2023); doi: 10.1063/5.0136918  
 Submitted: 29 November 2022 • Accepted: 13 February 2023 •  
 Published Online: 3 March 2023



Adam A. Dadey,<sup>1</sup> J. Andrew McArthur,<sup>2</sup> Abhilasha Kamboj,<sup>2</sup> Seth R. Bank,<sup>2</sup> Daniel Wasserman,<sup>2</sup>   
 and Joe C. Campbell<sup>1,a)</sup>

## AFFILIATIONS

<sup>1</sup>Department of Electrical and Computer Engineering, University of Virginia, Charlottesville, Virginia 22903, USA

<sup>2</sup>Department of Electrical and Computer Engineering, University of Texas, Austin, Texas 78758, USA

<sup>a)</sup>Author to whom correspondence should be addressed: [jcc7s@virginia.edu](mailto:jcc7s@virginia.edu)

## ABSTRACT

Mid-wavelength infrared (MWIR) detection is useful in a variety of scientific and military applications. Avalanche photodiodes can provide an advantage for detection as their internal gain mechanism can increase the system signal-to-noise ratio of a receiver. We demonstrate a separate absorption, charge, and multiplication avalanche photodiode using a digitally grown narrow-bandgap Al<sub>0.05</sub>InAsSb absorber for MWIR detection and a wide bandgap Al<sub>0.7</sub>InAsSb multiplier for low-excess-noise amplification. Under 2- $\mu\text{m}$  illumination at 100 K, the device can reach gains over 850. The excess noise factor of the device scales with a low  $k$ -factor of  $\sim 0.04$ . The unity-gain external quantum efficiency of the device attains a peak of 54% (1.02 A/W) at 2.35  $\mu\text{m}$  and maintains an efficiency of 24% (0.58 A/W) at 3  $\mu\text{m}$  before cutting off at  $\sim 3.5$   $\mu\text{m}$ . At a gain of 850, the device has a gain-normalized dark current density of 0.05 mA/cm<sup>2</sup>. This device achieves gains more than double that of the state-of-the-art InAs detectors and achieves gain-normalized dark current densities over two orders of magnitude lower than that of a previously reported MWIR Al<sub>0.15</sub>InAsSb-based detector.

© 2023 Author(s). All article content, except where otherwise noted, is licensed under a Creative Commons Attribution (CC BY) license (<http://creativecommons.org/licenses/by/4.0/>). <https://doi.org/10.1063/5.0136918>

## I. INTRODUCTION

The detection of mid-wavelength infrared (MWIR) light is of growing interest for a variety of scientific and military applications. The recent launch of the James Webb Space Telescope has sparked an increased interest in MWIR space imaging due to its inclusion of multiple MWIR capable detectors.<sup>1,2</sup> MWIR detection under 5  $\mu\text{m}$  is useful in gas sensing systems for environmental monitoring. In particular, the detection of water, methane, and ammonia is possible in the 3–3.5  $\mu\text{m}$  range.<sup>3</sup> In military applications, MWIR detection is used in night vision systems.<sup>4</sup>

The implementation of avalanche photodiodes (APDs) for the above applications can provide an advantage over traditional photodetectors as the internal gain mechanism can lead to higher receiver sensitivities due to an improved system signal-to-noise

ratio. The internal gain of APDs is achieved through the random process of impact ionization, creating a shot noise described by

$$\langle i_{\text{shot}}^2 \rangle = 2q(I_{\text{photo}} + I_{\text{dark}})\Delta f M^2 F(M), \quad (1)$$

where  $q$  is the elementary charge,  $M$  is the avalanche gain,  $I_{\text{photo}}$  and  $I_{\text{dark}}$  are the photo- and dark current,  $F(M)$  is the excess noise factor, and  $\Delta f$  is the measurement bandwidth. The excess noise factor in an APD can be represented using the simple local field model<sup>5</sup>

$$F(M) = kM + (1 - k)(2 - 1/M), \quad (2)$$

where  $k$  is defined as the ratio between  $\beta$ , the hole impact ionization coefficient, and  $\alpha$ , the electron impact ionization coefficient. Using this model, an ideal material would have a  $k$ -factor equal to zero,

in which the excess noise factor asymptotically approaches two with increasing gain.

HgCdTe is a widely used materials system for MWIR detection and amplification with devices exhibiting a high gain, up to 5300,<sup>6</sup> and near unity excess noise.<sup>7,8</sup> However, in addition to environmental concerns, HgCdTe is a difficult materials system to work with specifically regarding the low defect density crystal growth and p-type doping. There have been several recently proposed solutions to these problems; however, their implementations are still pending.<sup>9</sup> These growth difficulties have prompted the search for alternative materials systems for MWIR detection and amplification.

A popular III–V alternative to HgCdTe for detection below  $\sim 3.5\ \mu\text{m}$  is InAs as it too has a low excess noise factor near unity.<sup>10</sup> Several device implementations exist;<sup>11–13</sup> however, when operating at 77 K, in order to reduce the impact of band-to-band tunneling on dark current, the gain peaks at  $\sim 30$ . Operating at higher temperatures yields increased gains, up to  $\sim 300$ ; however, the dark current of these devices is poor due to band-to-band tunneling.<sup>10,14,15</sup> With InAs, there is a trade-off between the high gain and low dark current density. Additionally, InAs structures incorporate thick intrinsic regions, up to  $8\text{-}\mu\text{m}$  thick, to achieve gain while keeping the electric field low enough to suppress band-to-band tunneling. These thick intrinsic regions not only make it difficult to grow but also reduce the transit time bandwidth of the device.

Many of the aforementioned devices are relatively simple structures where absorption and multiplication occur in the same region. However, a separate absorption, charge, and multiplication (SACM) structure can be used to decouple the absorption and multiplication. This structure is useful as it alleviates band-to-band tunneling issues that plague narrow bandgap materials required to absorb MWIR light. In an SACM, the intermediate charge layer establishes an electric field profile that is high in the multiplier, promoting impact ionization, and low in the absorber, reducing the impact of band-to-band tunneling. With the proper materials system, these structures can be implemented to achieve high gain IR detection.

In recent years, digitally grown  $\text{Al}_x\text{In}_{1-x}\text{As}_y\text{Sb}_{1-y}$  (hereafter referred to as  $\text{Al}_x\text{InAsSb}$ ) lattice matched to GaSb<sup>16</sup> has been used to realize low-excess-noise, high-gain APDs<sup>17,18</sup> with  $k$ -factors of 0.01–0.05 and gains above 100 for visible and near-infrared (NIR) detection. Additionally, in this wavelength range,  $\text{Al}_x\text{InAsSb}$  layers have been successfully grown as a random alloy lattice matched to both InP and GaSb substrates for use in solar cells<sup>19,20</sup> and avalanche

photodiodes with a gain of 15 and  $k$ -factor of  $\sim 0.02$ .<sup>21</sup> SACM APDs have been demonstrated in the materials system for IR detection and amplification with cutoff wavelengths of  $1.7\text{-}\mu\text{m}$ ,<sup>22,23</sup>  $2.1\text{-}\mu\text{m}$ ,<sup>24</sup> and  $2.9\text{-}\mu\text{m}$ .<sup>25</sup> Specifically, the  $\sim 2.9\text{-}\mu\text{m}$  cutoff device in Ref. 24 has a unity-gain external quantum efficiency of 47% at  $2\ \mu\text{m}$  and can achieve gains up to 350.

In this paper, we present an SACM APD design using digitally grown  $\text{Al}_{0.05}\text{InAsSb}$  as the absorber for MWIR detection and digitally grown  $\text{Al}_{0.7}\text{InAsSb}$  as the multiplier for low excess noise amplification (hereafter referred to as  $3.5\text{-}\mu\text{m}$  cutoff SACM APD). This device achieves gains more than double that of the state-of-the-art InAs-based detectors and achieves gain-normalized dark current densities over two orders of magnitude lower than that of the previous MWIR  $\text{Al}_{0.15}\text{InAsSb}$ -based detector.<sup>25</sup> This device also achieves a longer wavelength cutoff than the InAs and previous MWIR  $\text{Al}_{0.15}\text{InAsSb}$  devices.

## II. DESIGN, GROWTH, AND FABRICATION

Epitaxial layers for the  $3.5\text{-}\mu\text{m}$  cutoff SACM APD, displayed in Fig. 1(a), were grown as a digital alloy via molecular beam epitaxy on an n-type GaSb substrate as discussed in a previous publication.<sup>16</sup> Figure 1(b) shows the simulated zero bias energy band diagram for the device with different regions of the device numbered. The simulation was performed using Ansys Lumerical CHARGE. Region 1 is the n-contact. Region 2 is the wide bandgap  $\text{Al}_{0.7}\text{InAsSb}$  multiplication layer. Region 3 contains an  $\text{Al}_{0.7}\text{InAsSb}$  p-type charge layer and an  $\text{Al}_{0.7-0.15}\text{InAsSb}$  bandgap grading region. By decreasing the Al concentration in  $\text{Al}_x\text{InAsSb}$ , the bandgap energy is reduced.<sup>16</sup> These layers in region 3 establish the electric field profile and provide a smooth transition between the multiplier and absorber. Region 4 is an  $\text{Al}_{0.15}\text{InAsSb}$  layer that helps prevent high electric field buildup in the narrow bandgap regions of the grading layer (region 3), reducing dark current contributions from band-to-band tunneling. A previous study<sup>25</sup> confirms the utility of this layer through a comparison of two SACM APD designs with and without this region. Region 5 is the  $\text{Al}_{0.05}\text{InAsSb}$  narrow bandgap absorber that has been lightly p-type doped to convert the doping polarity from n- to p-type, which in return helps prevent energy band sagging. Finally, region 6 acts as the p-contact as well as a diffusion barrier for electrons generated in the absorber. Figure 2 shows an x-ray diffraction pattern for the grown epitaxy shown in Fig. 1(a) with the GaSb substrate and  $\text{AlInAsSb}$  superlattice fringe peaks labeled.

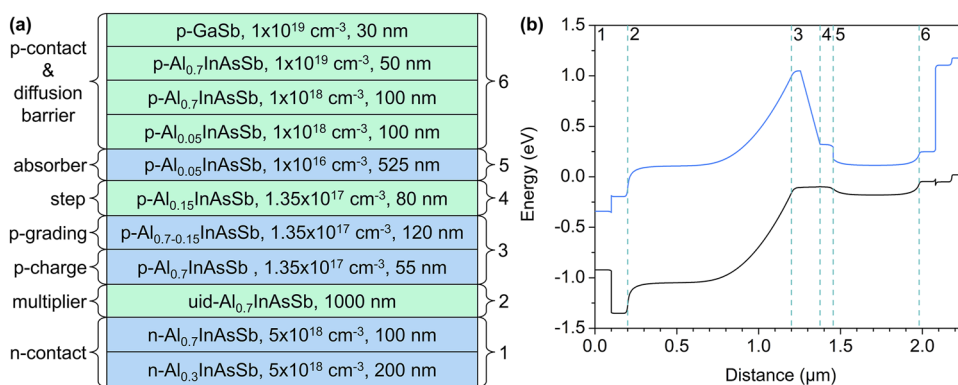


**FIG. 1.** (a) The epitaxial layer structure of the  $3.5\text{-}\mu\text{m}$  cutoff SACM APD and (b) the simulated zero bias energy band diagram with the corresponding regions numbered.

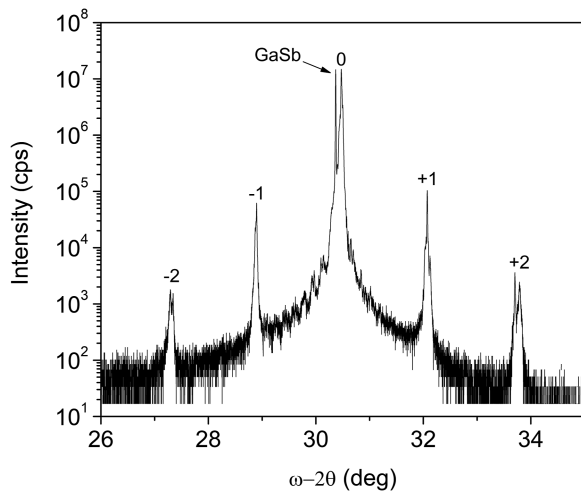


**FIG. 2.** X-ray diffraction pattern for the grown epitaxial layer structure shown in Fig. 1(a).

Circular mesas were defined using standard lithography techniques. Mesas were formed by first partially reactive ion etching with an inductively coupled plasma (ICP) through the low Al containing absorber and charge layers. A  $\text{Cl}_2:\text{N}_2$  (8 sccm/20 sccm) plasma was used with 300 W of ICP power. The remainder of the mesa was wet etched into the n-type  $\text{Al}_{0.3}\text{InAsSb}$  contact layer using a  $\text{C}_6\text{H}_8\text{O}_7:\text{H}_3\text{PO}_4:\text{H}_2\text{O}_2:\text{H}_2\text{O}$  (10 g:6 ml:3 ml:60 ml) solution. This wet etch also acts to clean up the surface damage caused during the dry etch. After forming the mesas, Ti/Au (10 nm/100 nm) contacts were deposited on both the p- and n-contact layers using e-beam evaporation. Finally, the mesa sidewalls were passivated with SU-8 to reduce surface leakage current.

### III. RESULTS

#### A. Capacitance–voltage characteristic

A capacitance–voltage (C–V) curve is shown for a 150- $\mu\text{m}$  diameter device in Fig. 3(a). Measurements were performed with an HP 3275A LCR meter at 1 MHz under blackout conditions in a cryogenic chamber cooled with liquid nitrogen to 100 K. In Fig. 3(a), the punch-through for the device is visible around 42 V of reverse

bias as indicated by the drop in capacitance. Around 46 V, the capacitance has leveled off, an indication that the device is fully depleted. Also included in Fig. 3(a) is a simulated C–V curve done using Ansys Lumerical CHARGE. This simulated C–V can be used to verify the doping concentration in the multiplier, absorber, and charge/grading regions. The doping concentration in the multiplier (region 2) and in the absorber (region 5) regions is  $\sim 2 \times 10^{15} \text{ cm}^{-3}$ . The doping concentration in the charge/grading region (regions 3 and 4) is  $\sim 1.28 \times 10^{17} \text{ cm}^{-3}$ . Figure 3(b) shows the calculated doping concentration profile vs depletion width for the C–V measured in Fig. 3(a). The depletion width was calculated assuming a parallel plate capacitor, where the overall relative permittivity used, 13.4, is a weighted average, based on the thickness, of the relative permittivity of  $\text{Al}_{0.7}\text{InAsSb}$  and  $\text{Al}_{0.05}\text{InAsSb}$ . The doping concentration calculation is detailed in a previous publication.<sup>26</sup> The charge region doping is visible between  $\sim 0.9$  and  $\sim 1.1 \mu\text{m}$  and has an average value of  $\sim 1.40 \times 10^{17} \text{ cm}^{-3}$ . The background concentration of the absorber is visible between  $\sim 1.1$  and  $\sim 1.7 \mu\text{m}$  and has a minimum value of  $\sim 2 \times 10^{15} \text{ cm}^{-3}$ . Both the doping value extracted from the simulation and the doping value calculated from the measured C–V are within 5% of the as-designed value. This difference is very reasonable considering the variation with growth parameters and measurement uncertainties.

#### B. Current–voltage characteristic

Current–voltage (I–V) curves were measured using an HP 4145 Semiconductor Parameter Analyzer in a cryogenic chamber cooled with liquid nitrogen. Figure 4 shows the dark current and photocurrent, under  $\sim 11 \text{ nW}$  and  $\sim 11 \mu\text{W}$  of 2- $\mu\text{m}$  illumination, for a 150- $\mu\text{m}$  diameter device measured at 100 K. A temperature-stabilized fiber-coupled laser diode was used with a fiber lens to focus the 2- $\mu\text{m}$  light to a spot size smaller than the mesa diameter to ensure no sidewall illumination. Under the lowest illumination, there are clearly two distinct steps in the photocurrent curve. The first step, around  $-34 \text{ V}$ , is likely caused when the device has depleted into the  $\text{Al}_{0.15}\text{InAsSb}$  barrier, region 4 in Fig. 1(b). Because the cutoff wavelength of  $\text{Al}_{0.15}\text{InAsSb}$  at 100 K is 2.94  $\mu\text{m}$ ,<sup>27</sup> the 2- $\mu\text{m}$  light was likely absorbed in this region, accounting for the increase in current. The second step, around  $-42 \text{ V}$ , occurs because the electric field has “punched through” into the absorber, allowing for injection of carriers from the absorber into the multiplier.

The gain of SACM APDs can be characterized after the electric field has punched through into the absorber. However, frequently,

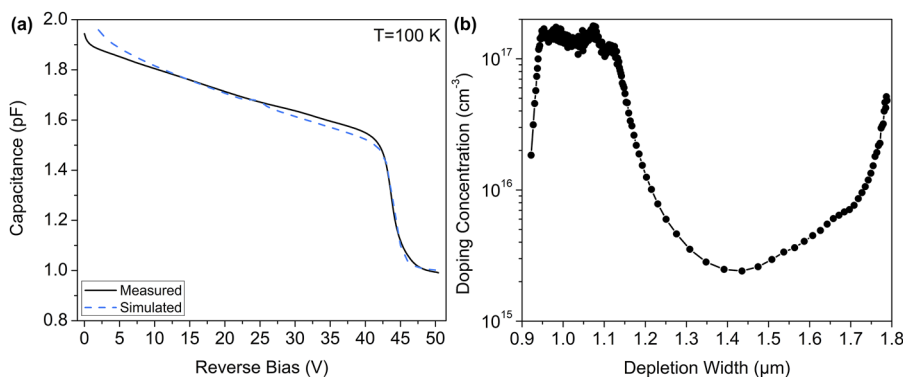


**FIG. 3.** (a) Measured capacitance–voltage characteristic, performed at 1 MHz, for a 150- $\mu\text{m}$  diameter device measured at 100 K and the simulated C–V curve; (b) the calculated doping concentration vs depletion width for the measured C–V curve in (a).

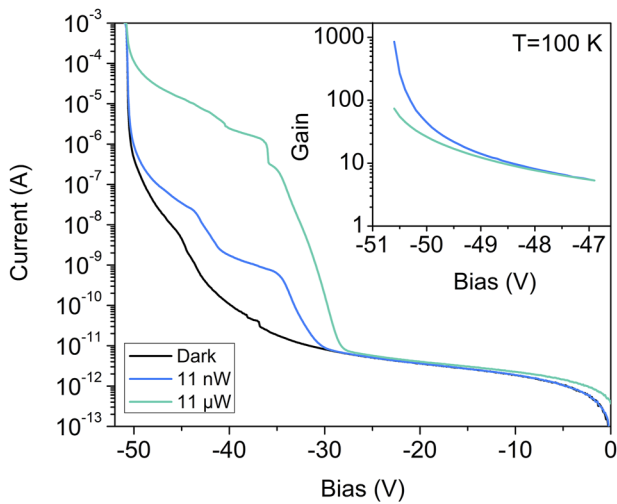


**FIG. 4.** Current–voltage characteristics at 100 K under  $\sim 11$  nW and  $\sim 11$   $\mu$ W of  $2\text{-}\mu\text{m}$  illumination with the inset showing the corresponding gains.

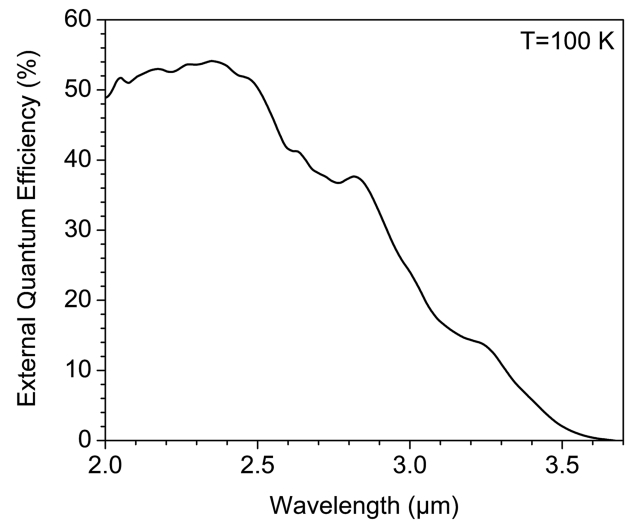


**FIG. 6.** Measured unity-gain external quantum efficiency of a  $250\text{-}\mu\text{m}$  diameter device at 100 K.

the electric field has built up in the multiplier such that the gain exceeds unity at punch-through. Using an excess noise measurement, the gain for an SACM APD can be determined at a certain bias after punch-through. This process is detailed in a previous publication.<sup>28</sup> The gains for the two intensities of  $2\text{-}\mu\text{m}$  illumination levels are plotted in the inset of Fig. 4. The difference in gain is caused by APD gain saturation, a well-known phenomenon in which the higher photocurrents in an APD cause a voltage drop across the series resistance of the device, lowering the bias across the APD and, in return, limiting the gain. Under the low incident light intensity ( $\sim 11$  nW), the maximum gain of this device is 850, which is more than two times that of the highest reported gain of InAs. The improved gain over InAs is likely due to the higher

achievable electric fields in the multiplication region. With InAs devices, the gain happens in a narrow bandgap region ( $\sim 0.35$  eV at 300 K), so the electric field must be kept low to prevent band-to-band tunneling. In this  $\text{Al}_x\text{InAsSb}$ -based structure, the gain is achieved in a wider bandgap region ( $\sim 1.1$  eV at 300 K), so higher electric fields are achievable without the onset of band-to-band tunneling. Additionally, at the maximum gain point,  $-50.6$  V, the photocurrent of the  $150\text{-}\mu\text{m}$  diameter device is  $\sim 9.3$   $\mu\text{A}$  and the dark current is  $\sim 7.4$   $\mu\text{A}$ .

### C. Excess noise factor

Excess noise measurements were performed with an Agilent 8973 noise figure analyzer in a cryogenic chamber. A  $150\text{-}\mu\text{m}$

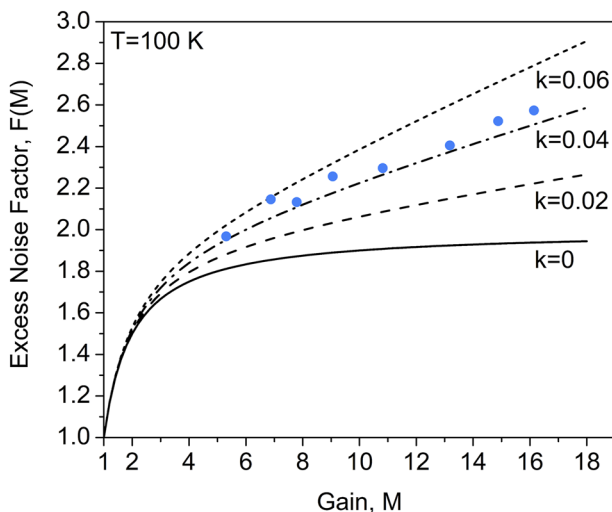


**FIG. 5.** Measured excess noise factor vs gain for a  $150\text{-}\mu\text{m}$  diameter device under  $517\text{-nm}$  illumination at 100 K.

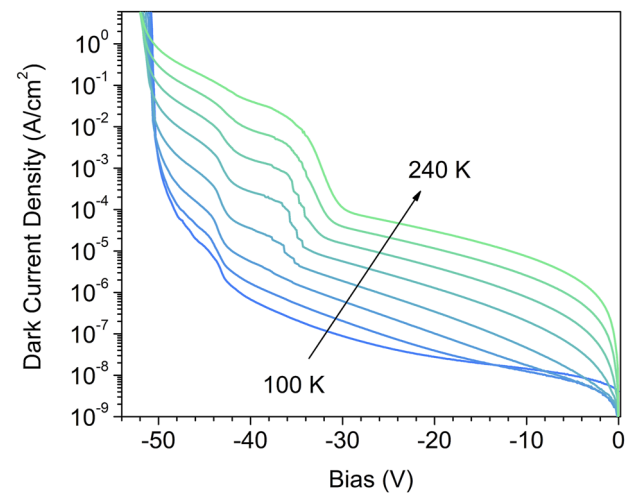


**FIG. 7.** Dark current density vs voltage for a  $150\text{-}\mu\text{m}$  diameter device at temperatures ranging from 100 to 240 K in 20-K increments.

**TABLE I.** 3.5- $\mu\text{m}$  cutoff SACM APD compared to other MWIR APDs. Boldface denotes the results of this work.

Reference	Material	Operating temperature (K)	Maximum gain	Gain-normalized DCD ( $\text{mA}/\text{cm}^2$ )	Cutoff wavelength ( $\mu\text{m}$ )
<b>This work</b>	<b><math>\text{Al}_{0.05}\text{InAsSb}</math></b>	<b>100</b>	<b>850</b>	<b>0.05</b>	<b><math>\sim 3.5</math></b>
11	InAs	77	27	0.005	$\sim 3$
13	InAs	200	330	0.4	$\sim 3.2$
24	$\text{Al}_{0.15}\text{InAsSb}$	100	380	6.0	$\sim 2.9$
6	HgCdTe	77	5300	0.001	$\sim 5$

diameter device was measured at 100 K under 517-nm illumination from a temperature-stabilized fiber-coupled laser diode. This wavelength was chosen to ensure complete absorption before the multiplier. Similar to the I–V measurements, the light was focused with a fiber lens to a spot size smaller than the mesa diameter. The results of this measurement are displayed in Fig. 5 along with the theoretical scaling of  $k = 0$  through  $k = 0.06$  using the local-field model.<sup>5</sup> The excess noise with this device scales with a low  $k$  of  $\sim 0.04$ , similar to the previously published results for  $\text{Al}_{0.7}\text{InAsSb}$  multipliers<sup>17,24</sup> and the known low  $k$  of  $\sim 0.01$  for Si.<sup>29,30</sup>

#### D. External quantum efficiency

Using the known gain of 5.3 at  $-46.9$  V, the unity-gain external quantum efficiency (EQE) for the device at 2- $\mu\text{m}$  is 49% (0.79 A/W). Further improvements can be explored using the equation for EQE,

$$\eta_{\text{ext}} = (1 - R)(1 - \exp(-\alpha W)), \quad (3)$$

where  $R$  is the surface reflection,  $\alpha$  is the absorption coefficient, and  $W$  is the depletion width. For this device, the top surface is GaSb, which has a relatively high reflectivity of  $\sim 35\%$  at 2  $\mu\text{m}$ .<sup>31</sup> With a proper 1% reflectivity anti-reflection (AR) coating, the unity-gain external quantum efficiency can be as high as  $\sim 74\%$  (1.2 A/W). Alternatively, if the absorber thickness is increased from 525 nm to 1  $\mu\text{m}$ , the external quantum efficiency can be increased to  $\sim 64\%$  (1.04 A/W). Compared to a previously demonstrated  $\text{Al}_{0.15}\text{InAsSb}$ -based structure,<sup>25</sup> this device has a unity-gain EQE of  $\sim 49\%$  at 2- $\mu\text{m}$  with a 525-nm thick absorber, whereas the previous structure exhibited a unity-gain EQE of  $\sim 47\%$  for a 1- $\mu\text{m}$  thick absorber. This device has a slightly higher unity-gain EQE with an absorber half as thick. This performance boost can be attributed to the higher absorption coefficient at 2- $\mu\text{m}$  due to the smaller bandgap of  $\text{Al}_{0.05}\text{InAsSb}$  compared to  $\text{Al}_{0.15}\text{InAsSb}$ .

The spectral response near cutoff was assessed using the double-modulated Fourier-transform IR (FTIR) spectroscopy at 100 K. A 250- $\mu\text{m}$  device was biased above the punch-through, at  $-46.9$  V, and the voltage drop across a 3-k $\Omega$  resistor was digitally processed to compute the spectral response of the device. Using the known unity-gain EQE at 2  $\mu\text{m}$  of 49% (0.79 A/W), the relative spectral response was converted to EQE and the result is plotted in Fig. 6. The peak unity-gain EQE of this detector is  $\sim 54\%$  (1.02 A/W) at  $\sim 2.35$   $\mu\text{m}$  and is  $\sim 24\%$  (0.58 A/W) at 3- $\mu\text{m}$ . Using a 1%-reflectivity AR coating could improve the unity-gain EQE of this detector to

$\sim 82\%$  (1.56 A/W) and  $\sim 37\%$  (0.9 A/W) at 2.35 and 3  $\mu\text{m}$ , respectively. This device has a 10-dB cutoff wavelength of  $\sim 3.4$   $\mu\text{m}$ , which is longer than the  $\sim 3$ - $\mu\text{m}$  cutoff of InAs and the  $\sim 2.9$ - $\mu\text{m}$  cutoff of the  $\text{Al}_{0.15}\text{InAsSb}$  structure in Ref. 24. In particular, this extended cutoff allows for the absorption of 3- $\mu\text{m}$  light.

#### E. Dark current density

The dark current density (DCD) vs voltage for a 150- $\mu\text{m}$  diameter device was measured from 100 to 240 K in 20-K increments using an HP 4145 semiconductor parameter analyzer in a cryogenic chamber. The results are displayed in Fig. 7. Using the gain from the inset of Fig. 4, the gain-normalized DCD at a gain of 10 at 100 K is  $\sim 0.03$   $\text{mA}/\text{cm}^2$ . At a gain of 850, the gain-normalized dark current density at 100 K is  $\sim 0.05$   $\text{mA}/\text{cm}^2$ . A previously reported InAs device with the highest gain of 27 at 77 K [10] has a gain-normalized DCD of  $\sim 0.005$   $\text{mA}/\text{cm}^2$ . The lower operating temperature and the increased bandgap of the InAs device likely account for its lower gain-normalized DCD. Compared to the previously reported MWIR  $\text{Al}_{0.15}\text{InAsSb}$ -based SACM<sup>25</sup> at 100 K, this device has a gain-normalized DCD over two orders of magnitude lower, 0.05  $\text{mA}/\text{cm}^2$  compared to 6  $\text{mA}/\text{cm}^2$ . The gain and gain-normalized DCD results for this device are summarized with the previously discussed III–V-based MWIR APDs in Table I. Additionally, a selected HgCdTe-based structure<sup>6</sup> is included for comparison.

#### IV. Conclusion

In this paper, we have demonstrated a high-gain, low-excess-noise, 3.5- $\mu\text{m}$  cutoff SACM APD based on the digitally grown  $\text{Al}_x\text{InAsSb}$  materials system. Under 2- $\mu\text{m}$  illumination, maximum gains in excess of 850 are achievable, more than double that of InAs. The unity-gain external quantum efficiency attains a peak of  $\sim 54\%$  (1.02 A/W) at  $\sim 2.35$   $\mu\text{m}$  and maintains an external quantum efficiency of  $\sim 24\%$  (0.58 A/W) at 3  $\mu\text{m}$ . Additionally, a low excess noise factor is achieved scaling with a  $k$  of  $\sim 0.04$ . At a gain of  $\sim 850$ , the gain-normalized dark current density is  $\sim 0.05$   $\text{mA}/\text{cm}^2$  at 100 K. This device achieves gains more than double that of the state-of-the-art InAs detectors and achieves dark current densities over two orders of magnitude lower than that of the previously best MWIR  $\text{Al}_{0.15}\text{InAsSb}$ -based detector. These results are promising for MWIR detection applications as the increased gains can lead to higher receiver sensitivities and offer an attractive III–V-based alternative to HgCdTe-based APDs.

## ACKNOWLEDGMENTS

This work was supported by Army Research Office and DARPA under Contract No. W911NF-17-1-0065 and DARPA under Contract No. W909MY-12-D-0008.

## AUTHOR DECLARATIONS

### Conflict of Interest

The authors have no conflicts to disclose.

## Author Contributions

**Adam A. Dadey:** Conceptualization (equal); Formal analysis (lead); Investigation (lead); Writing – original draft (lead). **J. Andrew McArthur:** Formal analysis (supporting); Investigation (supporting); Resources (supporting); Writing – review & editing (supporting). **Abhilasha Kamboj:** Formal analysis (supporting); Investigation (supporting); Methodology (supporting). **Seth R. Bank:** Conceptualization (equal); Funding acquisition (equal); Investigation (supporting); Project administration (equal); Resources (equal); Supervision (equal); Writing – review & editing (supporting). **Daniel Wasserman:** Formal analysis (supporting); Funding acquisition (supporting); Methodology (supporting); Project administration (supporting); Supervision (supporting); Writing – review & editing (supporting). **Joe C. Campbell:** Funding acquisition (lead); Project administration (lead); Supervision (lead); Writing – review & editing (equal).

## DATA AVAILABILITY

The data that support the findings of this study are available from the corresponding author upon reasonable request.

## REFERENCES

- <sup>1</sup>G. Bagnasco, M. Kolm, P. Ferruit, K. Honnen, J. Koehler, R. Lemke, M. Maschmann, M. Melf, G. Noyer, P. Rumler, J.-C. Salvignol, P. Strada, and M. T. Plate, in *Cryogenic Optical Systems and Instruments XII* (SPIE, 2007), pp. 174–187.
- <sup>2</sup>G. H. Rieke, M. E. Ressler, J. E. Morrison, L. Bergeron, P. Bouchet, M. García-Marín, T. P. Greene, M. W. Regan, K. G. Sukhatme, and H. Walker, *Publ. Astron. Soc. Pac.* **127**, 665 (2015).
- <sup>3</sup>D. Popa and F. Udrea, *Sensors* **19**, 2076 (2019).
- <sup>4</sup>M. Razeghi and B.-M. Nguyen, *Rep. Prog. Phys.* **77**, 082401 (2014).
- <sup>5</sup>R. J. McIntyre, *IEEE Trans. Electron Devices* **ED-13**, 164 (1966).
- <sup>6</sup>J. Rothman, G. Perrais, G. Destefanis, J. Baylet, P. Castelein, and J.-P. Chamonal, in *Infrared Technology and Applications XXXIII* (SPIE, 2007), pp. 475–484.
- <sup>7</sup>A. Singh, V. Srivastav, and R. Pal, *Opt. Laser Technol.* **43**, 1358 (2011).
- <sup>8</sup>A. Kerlain, G. Bonnouvrier, L. Rubaldo, G. Decaens, Y. Reibel, P. Abraham, J. Rothman, L. Mollard, and E. De Borniol, *J. Electron. Mater.* **41**, 2943 (2012).
- <sup>9</sup>W. Lei, J. Antoszewski, and L. Faraone, *Appl. Phys. Rev.* **2**, 041303 (2015).
- <sup>10</sup>W. Sun, Z. Lu, X. Zheng, J. C. Campbell, S. J. Maddox, H. P. Nair, and S. R. Bank, *IEEE J. Quantum Electron.* **49**, 154 (2013).
- <sup>11</sup>A. R. J. Marshall, C. H. Tan, M. J. Steer, and J. P. R. David, *IEEE Photonics Technol. Lett.* **21**, 866 (2009).
- <sup>12</sup>P. J. Ker, A. R. J. Marshall, A. B. Krysa, J. P. R. David, and C. H. Tan, *IEEE J. Quantum Electron.* **47**, 1123 (2011).
- <sup>13</sup>J. Huang, C. Zhao, B. Nie, S. Xie, D. C. M. Kwan, X. Meng, Y. Zhang, D. L. Huffaker, W. Ma, X. Meng, Y. Zhang, Y. Zhang, D. L. Huffaker, W. Ma, W. Ma, and W. Ma, *Photon. Res.* **8**, 755 (2020).
- <sup>14</sup>B. S. White, I. C. Sandall, X. Zhou, A. Krysa, K. McEwan, J. P. R. David, and C. H. Tan, *J. Lightwave Technol.* **34**, 2639 (2016).
- <sup>15</sup>W. Sun, S. J. Maddox, S. R. Bank, and J. C. Campbell, in *72nd Device Research Conference* (IEEE, 2014), pp. 47–48.
- <sup>16</sup>S. J. Maddox, S. D. March, and S. R. Bank, *Cryst. Growth Des.* **16**, 3582 (2016).
- <sup>17</sup>M. E. Woodson, M. Ren, S. J. Maddox, Y. Chen, S. R. Bank, and J. C. Campbell, *Appl. Phys. Lett.* **108**, 081102 (2016).
- <sup>18</sup>S. R. Bank, J. C. Campbell, S. J. Maddox, M. Ren, A. K. Rockwell, M. E. Woodson, and S. D. March, *IEEE J. Sel. Top. Quantum Electron.* **24**, 1 (2018).
- <sup>19</sup>S. Tomasulo, M. Gonzalez, M. P. Lumb, M. E. Twigg, I. Vurgaftman, J. R. Meyer, R. J. Walters, and M. K. Yakes, in *2019 IEEE 46th Photovoltaic Specialists Conference (PVSC)* (IEEE, 2019), pp. 3187–3190.
- <sup>20</sup>J. Kret, J. Tournet, S. Parola, F. Martinez, D. Chemisana, R. Morin, M. de la Mata, N. Fernández-Delgado, A. A. Khan, S. I. Molina, Y. Rouillard, E. Tournié, and Y. Cuminal, *Sol. Energy Mater. Sol. Cells* **219**, 110795 (2021).
- <sup>21</sup>S. H. Kodati, S. Lee, B. Guo, A. H. Jones, M. Schwartz, M. Winslow, N. A. Pfister, C. H. Grein, T. J. Ronningen, J. C. Campbell, and S. Krishna, *Appl. Phys. Lett.* **118**, 091101 (2021).
- <sup>22</sup>M. Ren, S. J. Maddox, M. E. Woodson, Y. Chen, S. R. Bank, and J. C. Campbell, *Appl. Phys. Lett.* **108**, 191108 (2016).
- <sup>23</sup>Y. Lyu, X. Han, Y. Sun, Z. Jiang, C. Guo, W. Xiang, Y. Dong, J. Cui, Y. Yao, D. Jiang, G. Wang, Y. Xu, and Z. Niu, *J. Cryst. Growth* **482**, 70 (2018).
- <sup>24</sup>A. H. Jones, S. D. March, S. R. Bank, and J. C. Campbell, *Nat. Photonics* **14**, 559 (2020).
- <sup>25</sup>A. H. Jones, S. D. March, A. A. Dadey, A. J. Muhowski, S. R. Bank, and J. C. Campbell, *IEEE J. Quantum Electron.* **58**, 1 (2022).
- <sup>26</sup>C. Frisk, Y. Ren, J. Olsson, T. Torndahl, F. Annoni, and C. Platzer-Bjorkman, *IEEE J. Photovoltaics* **7**, 1421 (2017).
- <sup>27</sup>A. A. Dadey, A. H. Jones, A. J. McArthur, E. Y. Wang, A. J. Muhowski, S. R. Bank, and J. C. Campbell, *Opt. Express* **30**, 27285 (2022).
- <sup>28</sup>H.-D. Liu, H. Pan, C. Hu, D. McIntosh, Z. Lu, J. Campbell, Y. Kang, and M. Morse, *J. Appl. Phys.* **106**, 064507 (2009).
- <sup>29</sup>T. Kaneda, H. Matsumoto, T. Sakurai, and T. Yamaoka, *J. Appl. Phys.* **47**, 1605 (1976).
- <sup>30</sup>H. Kanbe, T. Kimura, Y. Mizushima, and K. Kajiyama, *IEEE Trans. Electron Devices* **23**, 1337 (1976).
- <sup>31</sup>R. Ferrini, M. Patrini, and S. Franchi, *J. Appl. Phys.* **84**, 4517 (1998).